

# SCIENTIFIC REPORTS



OPEN

## Heat Transfer Enhancement During Water and Hydrocarbon Condensation on Lubricant Infused Surfaces

Daniel J. Preston , Zhengmao Lu , Youngsup Song , Yajing Zhao, Kyle L. Wilke , Dion S. Antao, Marcel Louis & Evelyn N. Wang

Vapor condensation is routinely used as an effective means of transferring heat or separating fluids. Dropwise condensation, where discrete droplets form on the condenser surface, offers a potential improvement in heat transfer of up to an order of magnitude compared to filmwise condensation, where a liquid film covers the surface. Low surface tension fluid condensates such as hydrocarbons pose a unique challenge since typical hydrophobic condenser coatings used to promote dropwise condensation of water often do not repel fluids with lower surface tensions. Recent work has shown that lubricant infused surfaces (LIS) can promote droplet formation of hydrocarbons. In this work, we confirm the effectiveness of LIS in promoting dropwise condensation by providing experimental measurements of heat transfer performance during hydrocarbon condensation on a LIS, which enhances heat transfer by  $\approx 450\%$  compared to an uncoated surface. We also explored improvement through removal of noncondensable gases and highlighted a failure mechanism whereby shedding droplets depleted the lubricant over time. Enhanced condensation heat transfer for low surface tension fluids on LIS presents the opportunity for significant energy savings in natural gas processing as well as improvements in thermal management, heating and cooling, and power generation.

Vapor condensation is routinely used as an effective means of transferring heat or separating fluids. Filmwise condensation is prevalent in typical industrial-scale systems, where the condensed fluid forms a thin liquid film due to the high surface energy associated with many industrial materials<sup>1</sup>. Conversely, dropwise condensation, where the condensate forms discrete liquid droplets which grow, coalesce, and shed, results in an improvement in heat transfer performance of an order of magnitude compared to filmwise condensation<sup>2–5</sup>. During water condensation, the dropwise mode is promoted with thin hydrophobic coatings<sup>4</sup>. However, low surface tension fluid condensates such as hydrocarbons pose a unique challenge since the typical hydrophobic condenser coatings used to shed water (surface tension  $\gamma \approx 73$  mN/m) often do not repel fluids with lower surface tensions ( $\gamma < 30$  mN/m). This is particularly relevant for natural gas processing applications<sup>6</sup>. Reentrant and doubly-reentrant surface designs have been proposed for repellency of low surface tension impinging droplets<sup>7,8</sup>, but these schemes are not useful during condensation when the impinging fluid can nucleate within the structures and subsequently render the surface hydrophilic<sup>9,10</sup>.

Meanwhile, lubricant infused surfaces (LIS) have found use in biological, lap-on-a-chip, anti-icing, and microfluidics applications, among others<sup>11–17</sup>. A LIS is comprised of a rough structured solid surface into which a lubricant is “infused,” or spontaneously wicked, and on which an impinging fluid ideally forms discrete droplets which easily shed from the surface. Recent work has indicated that LIS can promote formation of highly mobile droplets of low surface tension fluids, including hydrocarbons with surface tensions as low as pentane’s ( $\gamma \approx 16$  mN/m)<sup>18</sup>. LIS have also been shown to improve condensation heat transfer of water in the dropwise mode<sup>19</sup>. The natural combination of these two research directions is the use of LIS to promote dropwise condensation of low surface tension fluids. The behaviour during condensation of hydrocarbons and other low surface tension fluids on LIS has been reported qualitatively and suggests that LIS are a promising solution to promote dropwise condensation of hydrocarbons, but no experimentally-measured improvement in heat transfer has been reported<sup>20</sup>.

Department of Mechanical Engineering, Massachusetts Institute of Technology, Cambridge, Massachusetts, 02139, USA. Correspondence and requests for materials should be addressed to E.N.W. (email: [enwang@mit.edu](mailto:enwang@mit.edu))

	Water		Toluene	
	Advancing	Receding	Advancing	Receding
Bare Copper	≈0	≈0	≈0	≈0
Flat Hydrophobic Surface	104 ± 3	93 ± 3	29 ± 3	11 ± 5
Lubricant Infused Surface	108 ± 3	105 ± 3	58 ± 3	54 ± 3
Superhydrophobic Surface	171 ± 3	167 ± 3	≈0	≈0

**Table 1.** Advancing and receding contact angle (degrees) reported for water and toluene on the surfaces fabricated in this work. The superhydrophobic surface is the structured superhydrophobic CuO used to fabricate the LIS, but *without* lubricant added.

In the present work, we quantitatively confirmed the effectiveness of LIS in promoting dropwise condensation. First, we experimentally measured condensation heat transfer coefficients during water condensation in a controlled environmental chamber in the filmwise mode and during dropwise condensation on a flat hydrophobic surface and a LIS. Then, the heat transfer performance was determined during condensation of the hydrocarbon toluene ( $\gamma \approx 28$  mN/m) on bare and hydrophobic flat surfaces in the filmwise mode and on LIS-coated tubes in the dropwise mode at a range of supersaturations typical for natural gas processing applications. From these results, the heat transfer coefficient for hydrocarbon condensation on LIS was obtained experimentally. The  $\approx 450\%$  experimentally observed improvement in heat transfer for low surface tension fluids condensing on LIS presents the opportunity for significant energy savings not only in natural gas processing but also in applications such as thermal management, heating and cooling, and power generation.

## Experiment

In order to perform condensation experiments, we first fabricated tube condenser samples. The tube samples used to promote filmwise condensation of both water and toluene were bare copper (Cu) which was first solvent cleaned and then plasma cleaned. Commercially available oxygen-free Cu tubes (99.9% purity) with outer diameters  $D_{OD} = 6.35$  mm, inner diameters  $D_{ID} = 3.56$  mm, and lengths  $L = 131$  mm were obtained. Each Cu tube was cleaned in an ultrasonic bath with acetone for 10 minutes and rinsed with ethanol, isopropanol, and deionized (DI) water. Next, the tubes were dipped into a 2.0 M hydrochloric acid solution for 10 minutes to remove the native oxide film on the surface, then triple-rinsed with DI water and dried with clean nitrogen gas (99.9%, Airgas). Finally, within 30 minutes before any experiment using the bare Cu tubes, the samples were cleaned with argon plasma to remove adsorbed hydrocarbons which are known to render metal and metal oxide surfaces hydrophobic<sup>21–24</sup>.

The tube sample used to promote dropwise condensation of water was functionalized with a monolayer of the hydrophobic coating octadecyltrichlorosilane (OTS), but this sample was unable to promote dropwise condensation of toluene, as discussed later. A bare copper tube cleaned as described for the hydrophilic samples above was immersed in a 0.1% by volume solution of OTS ( $>90\%$ , Sigma-Aldrich) in n-hexane (99%, Sigma-Aldrich) for 5 minutes as detailed in prior work<sup>25,26</sup>. The coating had typical advancing/receding water contact angles of  $\theta_a/\theta_r \approx 104/93 \pm 3^\circ$  when measured on a flat reference surface.

The tube sample used to test condensation of both water and toluene on a LIS was a copper tube which was first coated with copper oxide (CuO) nanoblades etched following a well-known procedure<sup>27–32</sup>, then functionalized with a monolayer coating of trichloro(1H, 1H, 2H, 2H-perfluorooctyl)silane (TFTS) to reduce the surface energy<sup>33,34</sup>, and finally infused with the lubricant, Krytox GPL 101 fluorinated oil. CuO nanostructures were chosen in this study due to their suitability for copper condenser tubes; however, other options exist for fabrication of successful LIS, including silicon<sup>20</sup>, aluminium oxide<sup>35</sup>, and zinc oxide<sup>36</sup> micro- and nanostructures. To create the CuO nanostructures, a bare copper tube cleaned as described for the hydrophilic samples above was immersed into a hot ( $96 \pm 3^\circ\text{C}$ ) alkaline solution composed of  $\text{NaClO}_2$ ,  $\text{NaOH}$ ,  $\text{Na}_3\text{PO}_4 \cdot 12\text{H}_2\text{O}$ , and DI water (3.75 : 5 : 10 : 100 wt.%)<sup>27,33</sup>. During the oxidation process, a thin ( $\approx 300$  nm)  $\text{Cu}_2\text{O}$  layer was formed that then re-oxidized to form sharp, knife-like CuO oxide nanoblades with heights of  $h \approx 1$   $\mu\text{m}$ , solid fraction  $\varphi \approx 0.038$ , and roughness factor  $r \approx 4$ . The CuO structures were then functionalized with TFTS (Sigma-Aldrich), which was deposited from the vapor phase. Prior to silane deposition, the tube was oxygen plasma cleaned for 2 hours to remove organic contaminants from the surface. Once clean, the tube was immediately placed in a vacuum desiccator (06514-10, Cole Parmer) with a small amount of liquid TFTS. The desiccator was evacuated by a roughing pump for 2 minutes to a minimum pressure of  $\approx 2$  kPa. A valve was then closed to isolate the pump from the desiccator and the tube was held under vacuum ( $\approx 2$  kPa) for 10 minutes. The functionalized tube was then rinsed in ethanol and DI water and dried in a clean nitrogen stream (99.9%, Airgas). The TFTS coating had a typical advancing water contact angle of  $\theta_a \approx 119^\circ$  when measured on a flat reference surface and typical advancing/receding water contact angles of  $\theta_a/\theta_r \approx 171/167 \pm 3^\circ$  when measured on the functionalized nanostructured CuO surface. The surface was infused with lubricant by first placing a droplet of Krytox GPL 101 lubricant with an approximate diameter of 2 mm onto the surface and allowing it to spread, then using a clean nitrogen stream (99.9%, Airgas) to ensure that the lubricant had spread completely. The lubricant layer thickness and thermal resistance are examined in detail in the Supplementary Information, Section S7. Advancing and receding contact angle data for both water and toluene on all of the surfaces used in the present work are presented in Table 1.

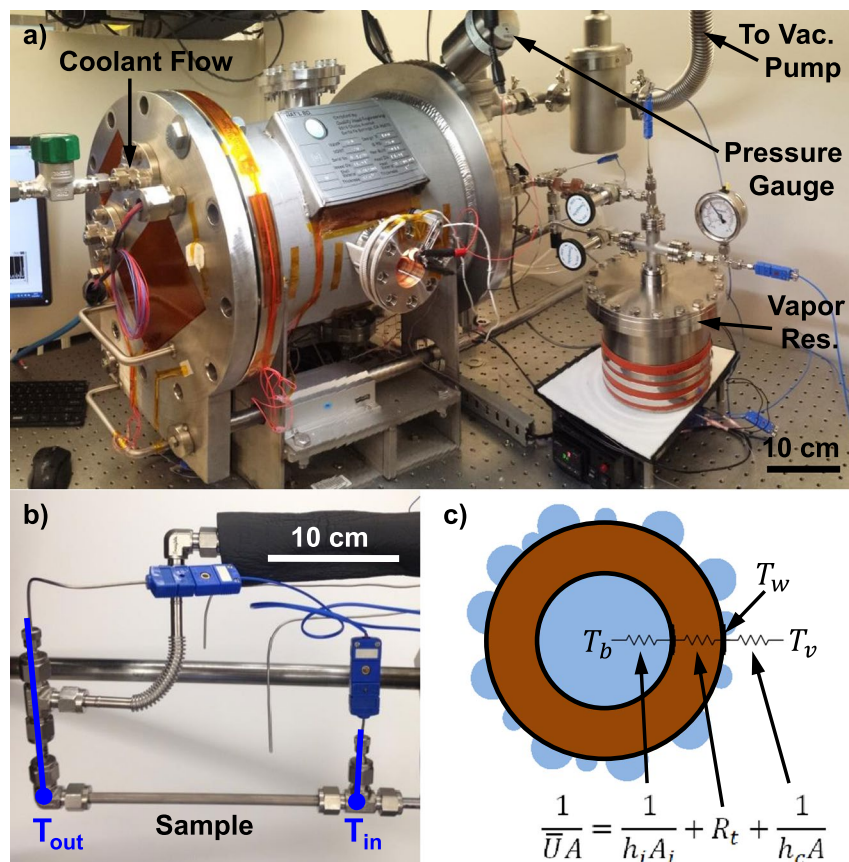


**Figure 1.** Environmental chamber with tube condenser sample to experimentally measure condensation heat transfer performance. The environmental chamber (a) was evacuated to  $<1$  Pa to remove noncondensable gases. Pure, degassed vapor was introduced into the chamber from a reservoir and condensed on the exterior surface of the tube sample (b), while the sample temperature was maintained by a flow of coolant through the tube interior. The condensation heat transfer coefficient,  $h_c$ , and subcooling,  $\Delta T = T_v - T_w$ , were determined from a thermal resistance network (c) for the tube sample.

## Results

Experiments were conducted in an environmental chamber (Fig. 1(a)). The chamber allowed the level of non-condensable gases (NCGs) to be controlled via a vacuum pump, including complete removal of NCGs from the system ( $<1$  Pa). Following removal of NCGs, pure, degassed vapor of the condensing fluid (either water or toluene) was introduced into the chamber from a heated, temperature-controlled canister and allowed to condense on the sample. The vapor pressure was varied from 2 to 5 kPa for water and from 2.5 to 5.5 kPa for toluene in order to set the subcooling,  $T_v - T_w$ , where  $T_v$  was measured and  $T_w$  was determined from the thermal resistance network shown in Fig. 1(c). Controlling for subcooling, the variation in heat transfer coefficient due to change in vapor pressure over this range is less than 5%<sup>37</sup>. The sample temperature was maintained with an internal flow of coolant water, where the sensible heating of the coolant fluid from the inlet to the outlet of the sample was characterized with thermocouples and used to determine the overall heat flux (Fig. 1(b)). The condensation heat transfer coefficient,  $h_c$ , and subcooling,  $\Delta T = T_v - T_w$ , were then calculated from the thermal resistance network shown in Fig. 1(c), where the thermal resistances of the internal flow and conduction through the tube wall are known. Operation of the environmental chamber and the procedure for calculation of the condensation heat transfer coefficient, including the error analysis, are detailed in the Supplementary Information.

We first characterized filmwise condensation of both water and toluene on the bare copper tubes and compared the results to Nusselt's falling-film theory in order to validate the experimental results<sup>1</sup>. The experimental results were in good agreement with Nusselt's model for both water and toluene (Fig. 2(a,b)). The slight over-prediction by the model (dotted lines) is attributed to the assumption that fluid reaching the bottom of the tube is immediately removed, while in reality the fluid accumulates at the bottom of the tube and eventually sheds as droplets, resulting in a higher average conduction resistance through the condensing fluid than in Nusselt's model.

We went on to characterize the condensation of water and toluene on the tube with a flat hydrophobic coating, where we observed that water underwent dropwise condensation (Fig. 3(a)) but toluene exhibited filmwise behaviour (Fig. 3(c)). While we initially observed the nucleation and growth of small, discrete droplets of toluene on the flat hydrophobic surface, at any appreciable heat flux, the toluene transitioned to filmwise condensation as can be expected for a condensate with low contact angle and non-negligible contact angle hysteresis, shown in detail in

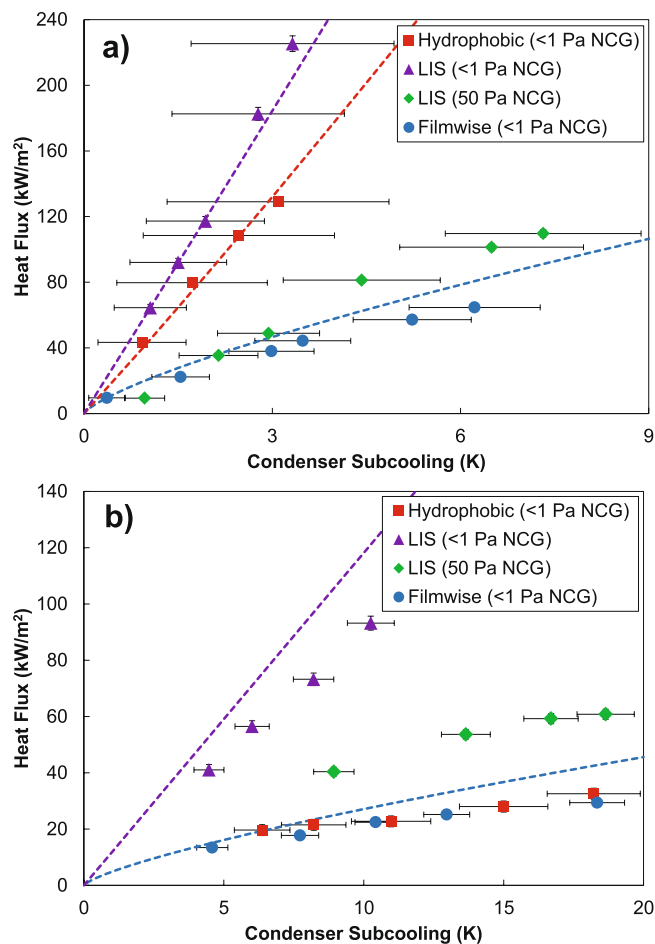


**Figure 2.** Heat flux as a function of condenser subcooling ( $\Delta T = T_v - T_w$ ) for water and toluene, with experimental results as points and model predictions as dashed lines. **(a)** Water is condensed onto a bare copper tube in the filmwise mode, a flat hydrophobic copper tube in the dropwise mode, and a LIS-coated copper tube in the dropwise mode in pure vapor and with 50 Pa of noncondensable gas (NCG) present in the chamber. **(b)** Toluene is condensed onto a bare copper tube in the filmwise mode and a LIS-coated copper tube in the dropwise mode in pure vapor and with 50 Pa of NCG present in the chamber. Toluene condensation on the flat hydrophobic copper tube resulted in the filmwise mode, evidenced by the agreement between the experimental data for this case and the model for filmwise condensation.

Figure S3 in the Supplementary Information<sup>4,38,39</sup>. This illustrates the difficulty of condensing low surface tension fluids on typical hydrophobic coatings. Meanwhile, the heat transfer performance for dropwise condensation of water outperformed filmwise condensation and was also in good agreement with a model based on individual droplet heat transfer integrated over a known droplet size distribution as shown in Fig. 2(a) (see Supplementary Information, Section S6 for model description)<sup>40</sup>.

Finally, we explored condensation of water and toluene on the LIS (Fig. 2). In a previous experiment in which water was condensed on a LIS performed by Xiao *et al.*, the condensation heat transfer coefficient was measured experimentally and reported to be 100% greater than that of dropwise condensation on a flat surface; however, the heat transfer coefficients reported in this work for dropwise condensation on both the flat hydrophobic surface and LIS were worse than the expected value for filmwise condensation calculated from Nusselt's model (see Supplementary Section S1)<sup>19</sup>. This study had included NCGs (30 Pa) in the chamber during the condensation heat transfer measurements, which are known to degrade heat transfer performance due to buildup of noncondensable gases at the condenser surface and an accompanying resistance due to vapor diffusion through the NCG layer<sup>3,4,41</sup>. While the NCGs were reported to serve the purpose of preventing evaporation of the lubricant<sup>19</sup>, we found that the vapor pressure of Krytox GPL 101 is much lower than 1 Pa, and therefore we were able to run experiments with virtually no NCG while still maintaining the presence of the Krytox lubricant on the surface. However, experiments were performed both without (i.e., <1 Pa) NCG and with 50 Pa NCG present to explore the effect of NCG on heat transfer performance and determine whether this could be the mechanism whereby Xiao *et al.* reported condensation heat transfer coefficients much lower than expected from modelling.

Condensation of both water and toluene on the LIS exhibited dropwise behaviour (Fig. 3(b,d)). In the presence of NCG, the heat transfer performance was only marginally better than filmwise condensation, rationalizing the result obtained by Xiao *et al.*<sup>19</sup>. When NCG was removed from the chamber, the heat transfer performance

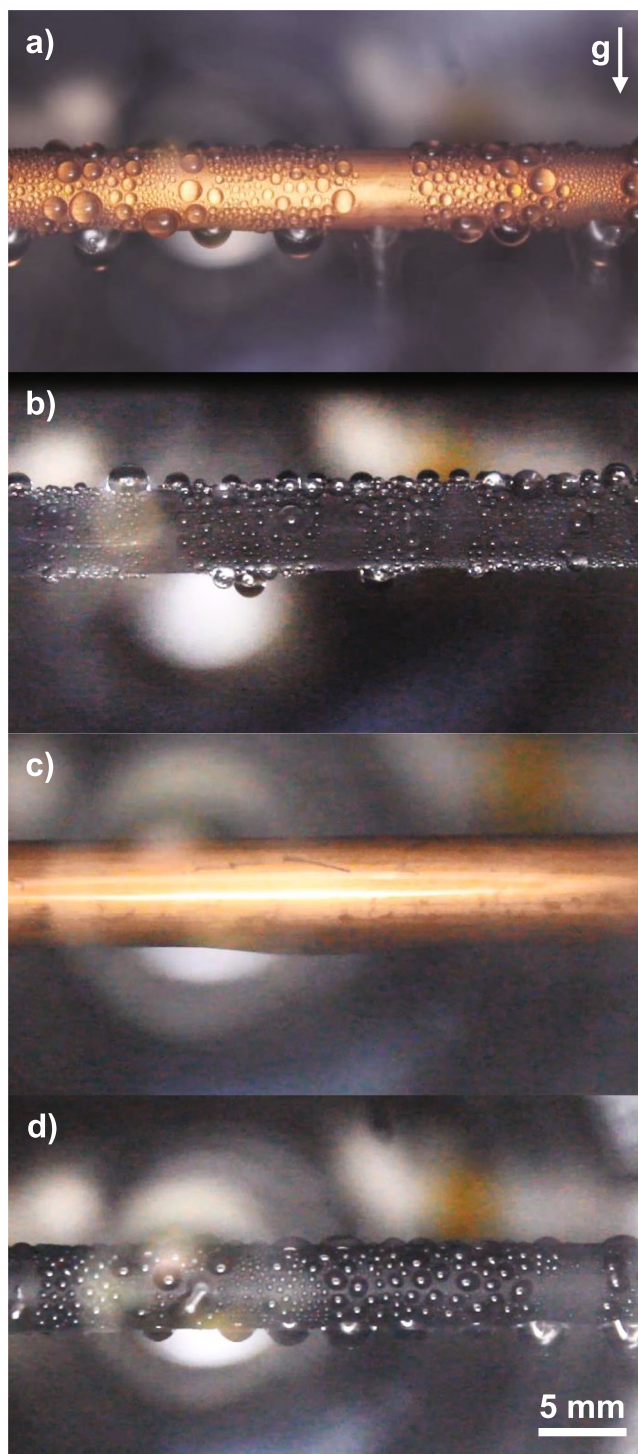


**Figure 3.** Images of condensation of water (**a,b**) and toluene (**c,d**). Water is condensed on the flat hydrophobic surface in (**a**) and on the LIS in (**b**). Toluene is condensed on the flat hydrophobic surface in (**c**) and on the LIS in (**d**). Droplet departure diameters were calculated from videos of condensation and used in the model to predict the expected dropwise heat transfer coefficients on the flat hydrophobic surface and the LIS (see Supplementary Information).

during water condensation exceeded that of dropwise condensation by  $\approx 30\%$  and filmwise condensation by  $\approx 400\%$ , as shown in Fig. 2 (note that the overlap in error bars for the experimental data points corresponding to dropwise condensation of water on the flat hydrophobic coating and the LIS does not indicate uncertainty that the flat coating may be outperforming the LIS, but rather that systematic experimental uncertainty may shift both sets of measurements in the same direction within the error bars). Meanwhile, toluene condensation on the LIS outperformed filmwise condensation by  $\approx 450\%$ , in good agreement with the prediction by Rykaczewski *et al.* of

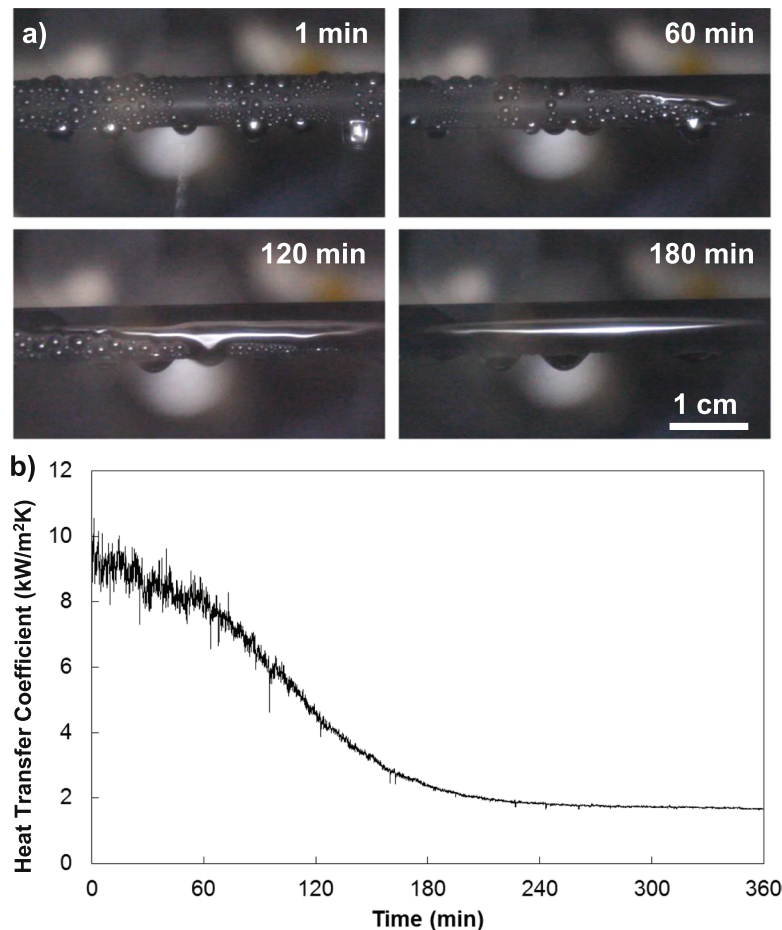


**Figure 4.** Toluene condensation on the LIS over time. Toluene initially exhibits dropwise condensation on the LIS, but within 1 hour the surface begins to transition to filmwise condensation, shown as a time-lapse sequence of images in (a). The lubricant was forced to the bottom of the condenser by shear force imparted by shedding droplets rendering the top of the condenser surface wettable by toluene. Correspondingly, the heat transfer coefficient degraded by approximately 78%, shown in (b). Upon rewetting the surface with lubricant, the surface could again shed discrete droplets of toluene, indicating that the failure was due to lubricant depletion and not structural damage.

a  $\approx 600\%$  enhancement for toluene condensing on a LIS based on an approximation considering a partial droplet size distribution<sup>20</sup>. Furthermore, experimental results for both water and toluene condensation on the LIS were in good agreement with the condensation heat transfer model accounting for a distribution of droplet sizes, where the droplet size distribution used in the model for LIS was adjusted according to recent work (see Supplementary Information Section S6)<sup>42,43</sup>.

The long-term performance of surface coatings is often a consideration when they are proposed for industrial applications. LIS are particularly concerning in this regard, as the lubricant may be depleted from the surface over time due to several mechanisms. If the droplets of condensate are “cloaked,” or covered in a thin layer of lubricant, they will carry lubricant with them during shedding and deplete the lubricant over time<sup>44–46</sup>. Another depletion mechanism is shearing of the lubricant, which may also occur due to droplet shedding as droplets slide over the LIS, causing accumulation of lubricant at the bottom of the condenser<sup>47,48</sup>. In order to test the failure mechanism of the LIS during hydrocarbon condensation, we continuously condensed toluene on the LIS over a time period of 6 hours. We found that the timescale for surface failure was on the order of 1 hour, evidenced by the time-lapse sequence of images in Fig. 4(a) and in agreement with another recent study on LIS which reported that low viscosity lubricants failed in less than 1 hour but did not explore the failure in further detail<sup>42</sup>. The condensation transitioned from dropwise to filmwise, with a corresponding decrease in heat transfer coefficient of  $\approx 78\%$  ( $=1-1/450\%$ ) shown in Fig. 4b. We also observed that the degradation began at the top of the condenser surface and slowly moved downwards. Since toluene is not cloaked by Krytox<sup>20,49</sup>, the droplet shearing effect<sup>47,48</sup> is primarily responsible for the LIS failure in this case as evidenced by the accumulation of lubricant at the base of the condenser over time.

## Discussion

Applying LIS to a condenser is shown here to be a viable approach to promote dropwise hydrocarbon condensation and improve the condensation heat transfer coefficient. This is not the only solution to improve heat transfer during condensation of low surface tension fluids; in some cases, it is also possible to modify the

functionalizations on flat condenser surfaces to lower the surface energy until droplet formation is energetically favorable<sup>20</sup>, particularly with fluorinated carbon chains<sup>50</sup>. However, geometric and chemical defects on solid surfaces result in contact angle hysteresis<sup>51,52</sup>, and a high level of contact angle hysteresis can cause a transition to filmwise condensation as heat flux increases<sup>4</sup>. Even traditional superhydrophobic surfaces are often unable to repel low surface tension fluids, as evidenced by the complete spreading of toluene over superhydrophobic CuO indicated in Table 1. The low contact angle hysteresis found on LIS therefore provides an advantage compared to flat or micro and nanostructured surfaces as it may allow continued shedding of droplets of low surface tension fluids at higher heat fluxes<sup>4,18,53</sup>.

LIS may prove more effective than flat or micro and nanostructured coatings at enhancing low surface tension fluid condensation heat transfer, but failure by depletion of the lubricant remains a critical concern. The lubricant can be depleted by departure of cloaked droplets, or, as observed in the present work, the lubricant can be depleted even in the absence of droplet cloaking due to shearing by sliding droplets. A potential solution to lubricant shearing could be the addition of barriers for lubricant flow as proposed by Wexler *et al.* in the context of fluid flow past a LIS<sup>47,48</sup>, or alternatively a suitable design of the solid structures on the surfaces to tune the capillary pressure and permeability governing lubricant return after shearing, which could draw from concepts proposed in literature on evaporation from wicking materials<sup>54,55</sup>. If justifiable in a given application, the lubricant could be replenished periodically as well to overcome the problem. The importance of NCG in condensation was also demonstrated in the present work, where less than 10% NCG was shown to eliminate the gain in performance obtained from promotion of dropwise condensation. This confirms previous results indicating the importance of even low levels of NCG on condensation performance<sup>41,56</sup>. Future experiments in this field should be carefully conducted in pure vapor to allow direct comparison between studies unless the target application requires NCG, such as in fog harvesting<sup>16</sup>.

Even in light of the challenges highlighted above that must be addressed before LIS will find practical use as a condenser coating, the enhancements in heat transfer coefficient versus filmwise condensation of 400% and 450% for water and toluene, respectively, suggest that LIS merit further exploration. Specifically, promotion of dropwise condensation of low surface tension fluids on LIS where flat coatings may not suffice due to contact angle hysteresis is a promising future direction. The demonstrated condensation heat transfer enhancement indicates more efficient natural gas processing as well as improved device thermal management, heating and cooling, and power generation are possible.

**Data availability.** All data generated or analysed during this study are included in this published article (and its Supplementary Information file).

## References

- Nusselt, W. The surface condensation of steam. *Z Ver Dtsch Ing* **60**, 569–575 (1916).
- Schmidt, E., Schurig, W. & Sellschopp, W. Condensation of water vapour in film- and drop form. *Z Ver Dtsch Ing* **74**, 544–544 (1930).
- Preston, D. J., Mafra, D. L., Miljkovic, N., Kong, J. & Wang, E. N. Scalable graphene coatings for enhanced condensation heat transfer. *Nano Lett* **15**, 2902–2909 (2015).
- Cho, H. J., Preston, D. J., Zhu, Y. & Wang, E. N. Nanoengineering materials for liquid–vapour phase-change heat transfer. *Nature Materials Reviews* **2**, 16092 (2016).
- Zhao, Y. *et al.* Effects of millimetric geometric features on dropwise condensation under different vapor conditions. *Int J Heat Mass Tran* **119**, 931–938 (2017).
- Seader, J. D. & Henley, E. J. *Separation process principles*. 2nd edn, (Wiley, 2005).
- Liu, T. Y. & Kim, C. J. Turning a surface superrepellent even to completely wetting liquids. *Science* **346**, 1096–1100, <https://doi.org/10.1126/science.1254787> (2014).
- Weisensee, P. B., Torrealba, E. J., Raleigh, M., Jacobi, A. M. & King, W. P. Hydrophobic and oleophobic re-entrant steel microstructures fabricated using micro electrical discharge machining. *J Micromech Microeng* **24**, 095020 (2014).
- Varanasi, K. K., Hsu, M., Bhate, N., Yang, W. S. & Deng, T. Spatial Control in the Heterogeneous Nucleation of Water. *Appl Phys Lett* **95**, 094101–094103 (2009).
- Enright, R., Miljkovic, N., Al-Obeidi, A., Thompson, C. V. & Wang, E. N. Condensation on Superhydrophobic Surfaces: The Role of Local Energy Barriers and Structure Length Scale. *Langmuir* **28**, 14424–14432, <https://doi.org/10.1021/La302599n> (2012).
- Epstein, A. K., Pokroy, B., Seminara, A. & Aizenberg, J. Bacterial biofilm provides persistent resistance to liquid wetting and gas penetration. *P Natl Acad Sci USA* **108**, 995–1000, <https://doi.org/10.1073/pnas.1011033108> (2011).
- Glavan, A. C. *et al.* Omniphobic “R-F Paper” Produced by Silanization of Paper with Fluoroalkyltrichlorosilanes. *Adv Funct Mater* **24**, 60–70, <https://doi.org/10.1002/adfm.201300780> (2014).
- Boreyko, J. B., Polizo, G., Datskos, P. G., Sarles, S. A. & Collier, C. P. Air-stable droplet interface bilayers on oil-infused surfaces. *P Natl Acad Sci USA* **111**, 7588–7593 (2014).
- Kim, P. *et al.* Liquid-Infused Nanostructured Surfaces with Extreme Anti-Ice and Anti-Frost Performance. *ACS Nano* **6**, 6569–6577 (2012).
- Lee, C., Kim, H. & Nam, Y. Drop Impact Dynamics on Oil-Infused Nanostructured Surfaces. *Langmuir* **30**, 8400–8407, <https://doi.org/10.1021/la501341x> (2014).
- Seo, D., Lee, J., Lee, C. & Nam, Y. The effects of surface wettability on the fog and dew moisture harvesting performance on tubular surfaces. *Sci Rep-Uk* **6**, 24276 (2016).
- Sett, S., Yan, X., Barac, G., Bolton, L. W. & Miljkovic, N. Lubricant-Infused Surfaces for Low-Surface-Tension Fluids: Promise versus Reality. *ACS Applied Materials & Interfaces* **9**, 36400–36408, <https://doi.org/10.1021/acsami.7b10756> (2017).
- Wong, T. S. *et al.* Bioinspired self-repairing slippery surfaces with pressure-stable omniphobicity. *Nature* **477**, 443–447 (2011).
- Xiao, R., Miljkovic, N., Enright, R. & Wang, E. N. Immersion Condensation on Oil-Infused Heterogeneous Surfaces for Enhanced Heat Transfer. *Sci Rep-Uk* **3**, 1988 (2013).
- Ryckaczewski, K. *et al.* Dropwise condensation of low surface tension fluids on omniphobic surfaces. *Sci Rep-Uk* **4**, 4158 (2014).
- Lundy, R. *et al.* Exploring the Role of Adsorption and Surface State on Hydrophobicity of Rare Earth Oxides. *ACS Appl Mater Interfaces* **9**, 13751–13760 (2017).
- Preston, D. J. *et al.* Effect of hydrocarbon adsorption on the wettability of rare earth oxide ceramics. *Appl Phys Lett* **105**, 011601 (2014).
- Fu, S. P. *et al.* On the wetting behavior of ceria thin films grown by pulsed laser deposition. *Appl Phys Lett* **110**, 081601 (2017).

24. Kulah, E. *et al.* Surface chemistry of rare-earth oxide surfaces at ambient conditions: reactions with water and hydrocarbons. *Sci Rep-Uk* **7** (2017).
25. He, Q. H., Ma, C. C., Hu, X. Q. & Chen, H. W. Method for Fabrication of Paper-Based Microfluidic Devices by Alkylsilane Self-Assembling and UV/O-3-Patterning. *Anal Chem* **85**, 1327–1331 (2013).
26. Asano, H. & Shiraiishi, Y. Development of paper-based microfluidic analytical device for iron assay using photomask printed with 3D printer for fabrication of hydrophilic and hydrophobic zones on paper by photolithography. *Anal Chim Acta* **883**, 55–60 (2015).
27. Nam, Y. & Ju, Y. S. Comparative Study of Copper Oxidation Schemes and Their Effects on Surface Wettability. *IMECE 2008: Heat Transfer, Fluid Flows, and Thermal Systems* **10**, 1833–1838 (2009).
28. Enright, R., Miljkovic, N., Dou, N., Nam, Y. & Wang, E. N. Condensation on Superhydrophobic Copper Oxide Nanostructures. *J Heat Trans-T Asme* **135** (2013).
29. Miljkovic, N., Preston, D. J., Enright, R. & Wang, E. N. Electric-field-enhanced condensation on superhydrophobic nanostructured surfaces. *Acs Nano* **7**, 11043–11054 (2013).
30. Miljkovic, N., Preston, D. J., Enright, R. & Wang, E. N. Electrostatic charging of jumping droplets. *Nat Commun* **4**, 2517 (2013).
31. Preston, D. J., Miljkovic, N., Enright, R. & Wang, E. N. Jumping droplet electrostatic charging and effect on vapor drag. *Journal of Heat Transfer* **136**, 080909 (2014).
32. Miljkovic, N., Preston, D. J., Enright, R. & Wang, E. N. Jumping-droplet electrostatic energy harvesting. *Appl Phys Lett* **105**, 013111 (2014).
33. Preston, D. J. *et al.* Electrowetting-on-dielectric actuation of a vertical translation and angular manipulation stage. *Appl Phys Lett* **109**, 244102 (2016).
34. Preston, D. J. *et al.* Electrowetting-on-dielectric actuation of a spatial and angular manipulation MEMS stage, in *2017 IEEE 30th International Conference on Micro Electro Mechanical Systems (MEMS)* 769–772 (IEEE, Las Vegas, 2017).
35. Kim, P., Kreder, M. J., Alvarenga, J. & Aizenberg, J. Hierarchical or Not? Effect of the Length Scale and Hierarchy of the Surface Roughness on Omniphobicity of Lubricant-Infused Substrates. *Nano Lett* **13**, 1793–1799, <https://doi.org/10.1021/Nl4003969> (2013).
36. Pacholski, C., Kornowski, A. & Weller, H. Self-assembly of ZnO: From nanodots, to nanorods. *Angew Chem Int Edit* **41**, 1188–1191, <https://doi.org/10.1002/1521-3773> (2002).
37. Miljkovic, N. *et al.* Jumping-Droplet-Enhanced Condensation on Scalable Superhydrophobic Nanostructured Surfaces. *Nano Lett* **13**, 179–187, <https://doi.org/10.1021/Nl303835d> (2013).
38. Rose, J. W. Dropwise condensation theory and experiment: a review. *P I Mech Eng a-J Pow* **216**, 115–128, <https://doi.org/10.1243/09576500260049034> (2002).
39. Wilmhurst, R. *Heat transfer during dropwise condensation of steam, ethane 1, 2 diol, aniline and nitrobenzene* Doctoral thesis, Queen Mary University of London, (1979).
40. Miljkovic, N., Enright, R. & Wang, E. N. Modeling and Optimization of Superhydrophobic Condensation. *Journal of Heat Transfer* **135**, 14 (2013).
41. Ma, X. H., Zhou, X. D., Lan, Z., Li, Y. M. & Zhang, Y. Condensation Heat Transfer Enhancement in the Presence of Non-Condensable Gas Using the Interfacial Effect of Dropwise Condensation. *Int J Heat Mass Tran* **51**, 1728–1737 (2008).
42. Weisensee, P. B. *et al.* Condensate droplet size distribution on lubricant-infused surfaces. *Int J Heat Mass Tran* **109**, 187–199 (2017).
43. Weisensee, P. B. *et al.* Erratum to “Condensate droplet size distribution on lubricant-infused surfaces” [Int. J. Heat Mass Transfer 109 (2017) 187–199]. *Int J Heat Mass Tran* **112**, 366 (2017).
44. Anand, S., Rykaczewski, K., Subramanyam, S. B., Beysens, D. & Varanasi, K. K. How droplets nucleate and grow on liquids and liquid impregnated surfaces. *Soft Matter* **11**, 69–80 (2015).
45. Smith, D. J. *et al.* Droplet mobility on lubricant-impregnated surfaces. *Soft Matter* **9**, 1772–1780 (2013).
46. Anand, S., Paxson, A. T., Dhiman, R., Smith, D. J. & Varanasi, K. K. Enhanced condensation on lubricant-impregnated nanotextured surfaces. *Acs Nano* **6**, 10122–10129 (2012).
47. Wexler, J. S., Jacobi, I. & Stone, H. A. Shear-Driven Failure of Liquid-Infused Surfaces. *Phys Rev Lett* **114**, 168301–168305 (2015).
48. Liu, Y., Wexler, J. S., Schonecker, C. & Stone, H. A. Effect of viscosity ratio on the shear-driven failure of liquid-infused surfaces. *Phys Rev Fluids* **1**, 074003 (2016).
49. Preston, D. J., Song, Y., Lu, Z., Antao, D. S. & Wang, E. N. Design of lubricant-infused surfaces. *ACS Applied Materials & Interfaces* **9**, 42383–42392 (2017).
50. Nishino, T., Meguro, M., Nakamae, K., Matsushita, M. & Ueda, Y. The lowest surface free energy based on -CF<sub>3</sub> alignment. *Langmuir* **15**, 4321–4323 (1999).
51. Raj, R., Enright, R., Zhu, Y. Y., Adera, S. & Wang, E. N. Unified Model for Contact Angle Hysteresis on Heterogeneous and Superhydrophobic Surfaces. *Langmuir* **28**, 15777–15788, <https://doi.org/10.1021/La303070s> (2012).
52. Lu, Z., Preston, D. J., Antao, D. S., Zhu, Y. & Wang, E. N. Coexistence of pinning and moving on a contact line. *Langmuir* **33**, 8970–8975 (2017).
53. Verheijen, H. J. J. & Prins, M. W. J. Reversible electrowetting and trapping of charge: Model and experiments. *Langmuir* **15**, 6616–6620 (1999).
54. Zhu, Y. Y. *et al.* Prediction and Characterization of Dry-out Heat Flux in Micropillar Wick Structures. *Langmuir* **32**, 1920–1927, <https://doi.org/10.1021/acs.langmuir.5b04502> (2016).
55. Zhu, Y. Y. *et al.* Surface Structure Enhanced Microchannel Flow Boiling. *J Heat Trans-T Asme* **138**, 091501 (2016).
56. Tanner, D. W., Pope, D., Potter, C. J. & West, D. Heat Transfer in Dropwise Condensation at Low Steam Pressures in Absence and Presence of Non-Condensable Gas. *Int J Heat Mass Tran* **11**, 181–182 (1968).

## Acknowledgements

We gratefully acknowledge funding support from the Abu Dhabi National Oil Company (ADNOC) with Dr. Abdullah Al Mahri as program manager and from the Office of Naval Research (ONR) with Dr. Mark Spector as program manager. D. J. Preston acknowledges funding received by the National Science Foundation Graduate Research Fellowship under Grant No. 1122374. Any opinion, findings, conclusions, or recommendations expressed in this material are those of the author(s) and do not necessarily reflect the views of the National Science Foundation. This work was performed in part at the Center for Nanoscale Systems (CNS), a member of the National Nanotechnology Infrastructure Network (NNIN), which is supported by the National Science Foundation under NSF award no. ECS-0335765. CNS is part of Harvard University.

## Author Contributions

D.J.P. and E.N.W. conceived the idea. All authors contributed to sample fabrication and experimental analysis. D.J.P. performed the condensation modeling for comparison to experiments. E.N.W. guided the work.

## Additional Information

**Supplementary information** accompanies this paper at <https://doi.org/10.1038/s41598-017-18955-x>.

**Competing Interests:** The authors declare that they have no competing interests.

**Publisher's note:** Springer Nature remains neutral with regard to jurisdictional claims in published maps and institutional affiliations.



**Open Access** This article is licensed under a Creative Commons Attribution 4.0 International License, which permits use, sharing, adaptation, distribution and reproduction in any medium or format, as long as you give appropriate credit to the original author(s) and the source, provide a link to the Creative Commons license, and indicate if changes were made. The images or other third party material in this article are included in the article's Creative Commons license, unless indicated otherwise in a credit line to the material. If material is not included in the article's Creative Commons license and your intended use is not permitted by statutory regulation or exceeds the permitted use, you will need to obtain permission directly from the copyright holder. To view a copy of this license, visit <http://creativecommons.org/licenses/by/4.0/>.

© The Author(s) 2018

Supplementary Information for:

# Heat Transfer Enhancement During Water and Hydrocarbon Condensation on Lubricant Infused Surfaces

*Daniel J. Preston, Zhengmao Lu, Youngsup Song, Yajing Zhao,*

*Kyle L. Wilke, Dion S. Antao, Marcel Louis, Evelyn N. Wang\**

Department of Mechanical Engineering, Massachusetts Institute of Technology,  
Cambridge, Massachusetts 02139, USA

*\*Corresponding author email: [enwang@mit.edu](mailto:enwang@mit.edu)*

## S1. Results from Xiao et al. Compared to Filmwise Condensation from Nusselt's Model

Xiao et al. reported that “the overall heat transfer coefficients on [dropwise condensation] surfaces in this work ( $h < 2\text{--}7 \text{ kW/m}^2\text{K}$ ) are much lower compared to pure vapor conditions [in previous work by Miljkovic et al.] ( $h < 12\text{--}13 \text{ kW/m}^2\text{K}$ )<sup>1</sup> due to the presence of NCGs acting as a diffusion barrier to the transport of water vapor towards the condensing surface.”<sup>2</sup> Therefore, the fact that the noncondensables (NCGs) would degrade heat transfer performance was recognized. Unfortunately, the data reported is the overall heat transfer coefficient including the tube wall and the chiller water flow, as opposed to the isolated condensation heat transfer coefficient. We can approximate the condensation heat transfer coefficient (including NCG effects) by assuming that the effective heat transfer coefficient of the non-condensing sections of the resistance network,  $h_{fixed}$ , namely, the tube wall and the chiller water flow, remains fixed between experiments (see Figure 1 in the main text for a schematic of the resistance network):

$$h_{fixed} = \left( \frac{1}{h_{overall}} - \frac{1}{h_{cond}} \right)^{-1} = \left( \frac{1}{12 \text{ kW/m}^2\text{K}} - \frac{1}{60 \text{ kW/m}^2\text{K}} \right)^{-1} = 15 \text{ kW/m}^2\text{K} \quad (\text{S1})$$

where  $h_{overall}$  is taken from the earlier work by Miljkovic et al. using the same experimental setup to characterize dropwise condensation and  $h_{cond}$  is the heat transfer coefficient of dropwise condensation reported in that work.<sup>1</sup> Now we compare  $h_{fixed}$  with the range of overall heat transfer coefficients reported by Xiao et al.,  $2\text{--}7 \text{ kW/m}^2\text{K}$ , and we see that the thermal resistance of the condensation with NCGs is the dominant resistance in the network in this scenario:

$$\frac{R_{cond}}{R_{overall}} = \frac{h_{overall}}{h_{cond}} = \frac{h_{overall}}{\left( \frac{1}{h_{overall}} - \frac{1}{h_{fixed}} \right)^{-1}} = 53\% \text{ to } 87\% \quad (\text{S2})$$

Rearranging this equation, we can determine the  $h_{cond}$  including the effect of NCG for any given  $h_{overall}$  reported in Figure 4 of Xiao et al. using Equation S3 here:

$$h_{cond} = \left( \frac{1}{h_{overall}} - \frac{1}{h_{fixed}} \right)^{-1} \quad (S3)$$

Next, assuming a constant wall temperature,  $T_w$ , across all experiments of 17 °C, determined from the supersaturation of 1.6 at the maximum vapor pressure plotted in Xiao et al.'s Figure 4, we can also determine the vapor temperature,  $T_v$ , at each vapor pressure for a saturated mixture,

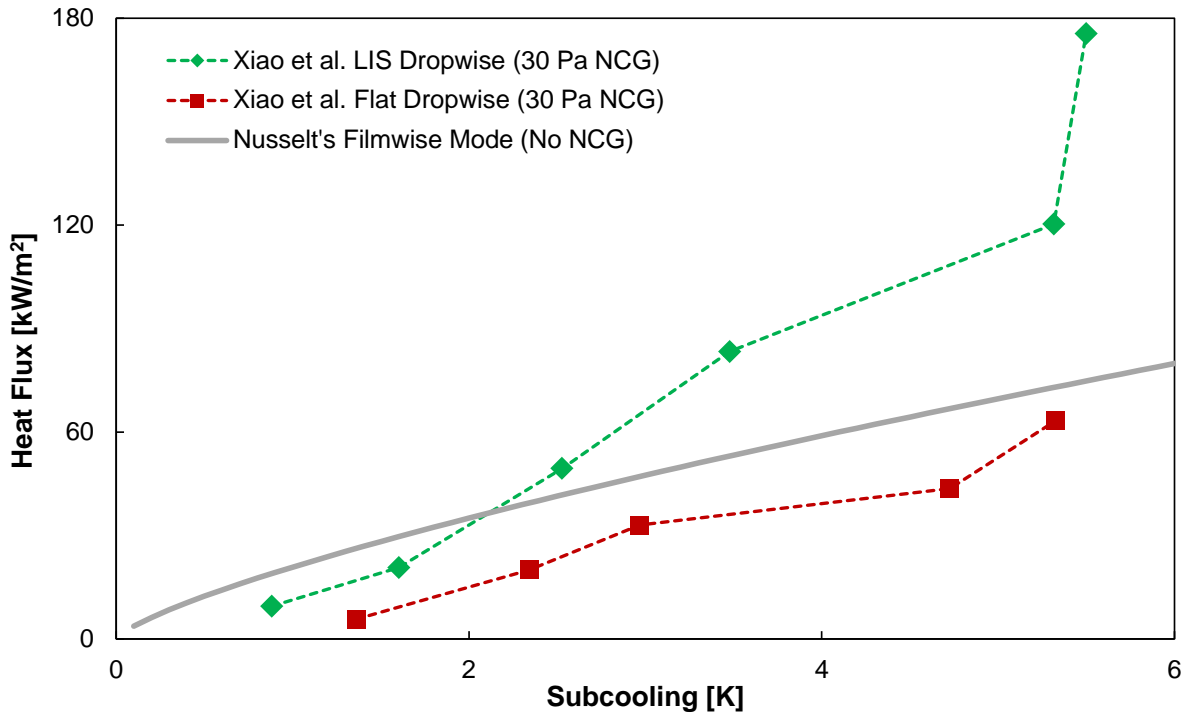


**Figure S1.** Adjusted and replotted data from Xiao et al. shows heat flux vs. condenser subcooling. The 30 Pa NCG in the system degrades the heat transfer performance of the dropwise condensation to approximately that of the expectation for filmwise condensation.

and from these two temperatures the subcooling is known. The subcooling and the condensation heat transfer coefficient can be combined to determine the heat flux for each data point. Finally, plotting the heat flux versus the subcooling for each data point yields the result shown in Figure S1, where the heat transfer is comparable to that which would be expected from filmwise condensation.

### **S2. Droplet Departure Size Characterization**

The average droplet departure size was calculated using imaging analysis performed on videos of condensation on the different surfaces with at least 20 departure events observed for each sample. The results are shown in Table S1.

**Table S1.** Average droplet departure diameters.

	Average Diameter (mm)	Standard Deviation (mm)
Water on Flat Hydrophobic Surface	2.92	0.42
Water on LIS	1.23	0.34
Toluene on LIS	2.12	0.23

### **S3. Condensation Chamber Setup**

The custom environmental chamber used for this work consists of a stainless steel frame with a door (sealed with a rubber gasket), two viewing windows, and apertures for various components. Resistive heater lines were wrapped around the exterior of the chamber walls to prevent condensation at the inside walls and then insulated on the exterior walls. The output power of the

resistive heater lines was controlled by a voltage regulator. Two insulated stainless steel water flow lines (Swagelok) were fed into the chamber to supply cooling water to the chamber from a large capacity chiller.

A secondary stainless steel tube line was fed into the chamber that served as the flow line for the incoming vapor supplied from a heated steel reservoir. The vapor line was wrapped with a rope heater (60 W, Omega) and controlled by a power supply. The vapor reservoir was wrapped with another independently-controlled heater (120 W, Omega) and insulated to limit heat losses to the environment. The access tubes were welded to the vapor reservoir, each with independently-controlled valves. The first valve (Diaphragm Type, Swagelok), connecting the bottom of the reservoir to the ambient, was used to fill the reservoir with the condensing fluid. The second valve (BK-60, Swagelok), connecting the top of the reservoir to the inside of the chamber, provided a path for vapor inflow. K-type thermocouples were located along the length of the vapor reservoir to monitor temperature.

A bellows valve (Kurt J. Lesker) was attached to the chamber to serve as a leak port between the ambient and inside of the chamber. In order to monitor temperatures within the chamber, T-type thermocouple bundles were connected through the chamber apertures *via* a thermocouple feed through (Kurt J. Lesker). A pressure transducer (925 Micro Pirani, MKS) was attached to monitor pressure within the chamber. The thermocouple bundles and the pressure transducer were both electrically connected to an analog input source (RAQ DAQ, National Instruments), which was interfaced to a computer for data recording. A second bellows valve (Kurt J. Lesker) was integrated onto the chamber for the vacuum pump, which brought down the chamber to

vacuum conditions prior to vapor filling. A liquid nitrogen cold trap was incorporated along the line from the chamber to the vacuum which served to remove any moisture from the pump-down process and ultimately assisted in yielding higher quality vacuum conditions. A tertiary bellows valve (Kurt J. Lesker) was integrated on a T fitting between the vacuum pump and liquid nitrogen reservoir to connect the vacuum line to the ambient to release the vacuum line to ambient conditions once pump-down was achieved. In order to visually capture data, a digital SLR camera (Canon EOS 50D) was placed in line with the viewing window on the chamber.

The setup used to run experiments inside the chamber is shown in Figure 1(a) in the main text. Stainless steel tube lines (1/4", Swagelok) were connected to the external water flow lines (Figure 1(b) in the main text). T-connection adapters (Swagelok) with bore through Ultra-Torr fittings (Swagelok) were used to adapt T-type thermocouple probes (Omega) at the water inlet and outlet.

#### **S4. Condensation Procedure**

For each experimental trial, a set of strict procedures was followed to ensure consistency throughout the experiments. The first step of the process was to turn on the voltage regulator to heat up the environmental chamber walls, which prevented condensation on the chamber walls. Simultaneously, the vapor reservoir was filled with approximately 2 liters of either DI water or toluene. After opening the vapor inflow valve and closing the vapor release valve, the rope heater around the vapor reservoir was turned on with the heater controller set to maximum output (1200 W). Then the rope heater connected to the vapor inflow valve was turned on. The temperature of the reservoir was monitored with the installed thermocouples; the temperature at

the top of the reservoir was higher than that of the middle/bottom of the reservoir due to the water thermal mass present at the middle/bottom section. Hence, we ensured that the regions of the reservoir of higher thermal capacity were brought to a sufficiently high temperature for boiling. During the boiling process, aluminum foil was placed on the bottom surface of the inner chamber to collect any of the liquid leaving the vapor inflow line. Once boiling was achieved and the internal thermocouple on the reservoir was 5°C above the boiling point for at least 10 minutes, the vapor inflow valve was closed. The excess fluid that spilled inside the chamber during de-gassing of the reservoir was removed.

In order to install the samples onto the rig, the Swagelok female adapters at the ends of the tube samples were connected to the male connectors on the rig. Before installing the entire sample setup in the chamber, all adapters/connecters were tightened to ensure that there were no leaks that could affect vacuum performance. Finally, the bellows tubes (for the chiller water inflow/outflow) were connected to the chiller water lines.

The next step was to begin the vacuum pump-down procedure. Initially, the liquid nitrogen cold trap was filled to about half capacity. The ambient exposed valves connecting the chamber and the vacuum pump were both closed and the valve connected to the liquid nitrogen cold trap was opened. The vacuum pump was then turned on, initiating the pump-down process. The pressure inside the chamber was monitored during the pump-down process. This process took approximately one hour in order to achieve the target vacuum conditions ( $0.5 \text{ Pa} < P < 1 \text{ Pa}$ ). The experimental operating pressure of non-condensable was set to be a maximum of 0.25% of the operating pressure. Non-condensable gas content of above 0.5% (pressure) has been shown

to significantly degrade performance during dropwise condensation.<sup>3</sup> In our experiments, extreme care was taken to properly de-gas the vacuum chamber and vapor reservoir prior to experimental testing. In addition, the chamber leak rate was characterized prior to each run in order to estimate the maximum time available for acquiring high fidelity data with non-condensable content of less than 0.25%.

The setup of the chiller water flow-loop is described as follows: the water pump reservoir was filled and turned on to a flow rate of 5 L/min. The flow rate was monitored with the flow meter integrated in the inflow water line. In order to bring the chilled water into the flow loop and to the tube sample, the external chilled water lines were opened.

Prior to beginning experiments, the camera was turned on for visual imaging of the sample during condensation. Afterwards, the rope heater around the water reservoir was turned off and the vapor inflow valve was slowly turned open until the operating pressure was reached. Steady state conditions were typically reached after 2 minutes of full operation.

## **S5. Heat Transfer Coefficient and Error Propagation**

An energy balance was applied to the tube sample to determine the overall condensation heat transfer by calculating the change in enthalpy of the chiller water flowing inside the tube:

$$Q = \dot{m}c_p(T_{out} - T_{in}) \quad (S4)$$

where  $Q$  is the overall condensation heat transfer rate,  $\dot{m}$  is the chiller water mass flow rate,  $c_p$  is the chiller water specific heat, and  $T_{in}$  and  $T_{out}$  are the tube condenser inlet and outlet temperatures, respectively. From the overall heat transfer rate, we calculated the heat flux by dividing by the condenser surface area:

$$q'' = Q/A = \dot{m}c_p(T_{out} - T_{in})/A \quad (S5)$$

where  $A$  is the surface area of the outer tube surface ( $A = 2\pi rL$ , where  $r = 3.175$  mm,  $L = 13.1$  cm). The temperature difference between the chiller water and vapor far from the tube sample was also determined, represented here as the log mean temperature difference (LMTD) to account for the change in temperature of the chiller water along the tube length:

$$\Delta T_{LMTD} = \frac{(T_v - T_{in}) - (T_v - T_{out})}{\ln\left(\frac{T_v - T_{in}}{T_v - T_{out}}\right)} \quad (S6)$$

where  $T_v$  is the temperature of the surrounding vapor far from the tube sample ( $T_v = T_{sat}(P_v)$ ). From the overall condensation heat transfer and the log mean temperature difference, the overall heat transfer coefficient,  $\bar{U}$ , was determined:

$$\bar{U} = \frac{Q}{A\Delta T_{LMTD}} = \frac{\dot{m}c_p(T_{out} - T_{in})}{A\Delta T_{LMTD}} \quad (S7)$$

where  $A$  is the surface area of the outer tube surface ( $A = 2\pi rL$ , where  $r = 3.175$  mm,  $L = 13.1$  cm). Note that the overall heat transfer coefficient is a function of only the product of experimentally measured parameters raised to powers. Therefore, the error associated with  $\bar{U}$  is calculated as follows:

$$E_{\bar{U}} = \bar{U} \sqrt{\left(\frac{E_{\dot{m}}}{\dot{m}}\right)^2 + \left(\frac{E_{(T_{out}-T_{in})}}{(T_{out}-T_{in})}\right)^2 + \left(\frac{-E_A}{A}\right)^2 + \left(\frac{-E_{\Delta T_{LMTD}}}{\Delta T_{LMTD}}\right)^2} \quad (S8)$$

The condensation heat transfer coefficient can be extracted from  $\bar{U}$  by considering a series of thermal resistances that sum to  $\bar{U}$  and isolating the resistance associated with condensation:

$$\frac{1}{\bar{U}A} = \frac{1}{h_i A_i} + R_t + \frac{1}{h_c A} \quad (S9)$$

Rearranging to solve explicitly for  $h_c$ :

$$h_c = \left(\frac{1}{\bar{U}} - \frac{A}{h_i A_i} - R_t A\right)^{-1} \quad (S10)$$

where  $A_i$  is the surface area on the inner surface of the tube ( $A_i = 2\pi r_i L$ ),  $R_t$  is the thermal resistance of the tube ( $R_t = \ln(r/r_i)/(2\pi k_t)$ ,  $k_t$  is the tube material thermal conductivity), and the internal heat transfer coefficient,  $h_i$ , is determined from the Gnielinski correlation for pipe flow:

$$h_i = \left(\frac{k_i}{2r_i}\right) \frac{(f/8)(Re - 1000)Pr}{1 + 12.7(f/8)^{1/2}(Pr^{2/3} - 1)} \quad (\text{S11})$$

$$f = (0.790 \ln Re - 1.64)^{-2} \quad (\text{S12})$$

$$Re = \frac{\rho v(2r_i)}{\mu} \quad (\text{S13})$$

where  $f$  is the friction factor,  $Re$  is the Reynolds number,  $Pr$  is the Prandtl number,  $\rho$  is the chiller water density,  $k_i$  is the chiller water thermal conductivity, and  $\mu$  is the chiller water dynamic viscosity. Solving for  $h_i$  and substituting into the above Equation S10 allows for determination of  $h_c$ . Once  $h_c$  is known, the condenser surface subcooling is determined as follows:

$$\Delta T = T_v - T_w = \frac{q''}{h_c} \quad (\text{S14})$$

As  $h_c$  is not a simple function of a product of powers, the error is determined as a function of the first partial derivatives of  $h_c$  with respect to its components.

$$E_{h_c} = h_c \sqrt{\left(\frac{\partial h_c}{\partial h_i} E_{h,i}\right)^2 + \left(\frac{\partial h_c}{\partial \bar{U}} \frac{E_{\bar{U}}}{\bar{U}}\right)^2} \quad (\text{S15})$$

$$\frac{\partial h_c}{\partial h_i} = \frac{-(A/A_i)\bar{U}^2}{(h_i - (A/A_i)\bar{U} - R_t A \bar{U} h_i)^2} \quad (\text{S16})$$

$$\frac{\partial h_c}{\partial \bar{U}} = \frac{h_i^2}{(h_i - (A/A_i)\bar{U} - R_t A \bar{U} h_i)^2} \quad (\text{S17})$$

The error in  $\bar{U}$  was determined in Equation S8 and the error in  $h_i$  was estimated as 10% associated with the Gnielinski correlation.<sup>4</sup> Table S2 below summarizes the uncertainty associated with each experimental measurement.

**Table S2. Uncertainties corresponding to experimental measurements.**

<b>Experimental Measurement</b>	<b>Uncertainty</b>
Chiller water temperature difference ( $T_{out} - T_{in}$ )	0.1K
Saturated vapor pressure ( $P_v$ )	1%
Saturated vapor temperature ( $T_v$ )	$T_{sat}(1.01(P_v)) - T_{sat}(P_v)$
Chiller water mass flow rate ( $\dot{m}$ )	2%
Sample surface area ( $A$ )	2%
Gnielinski correlation heat transfer coefficient ( $h_i$ )	10%

## S6. Modeling of Heat Transfer Coefficient

To model dropwise condensation,  $h_{c,d}$  was obtained by incorporating the individual droplet heat transfer with droplet size distribution:<sup>5</sup>

$$h_{c,d} = \frac{q''}{\Delta T} = \frac{1}{\Delta T} \left( \int_{R^*}^{R_e} q(R)n(R)dR + \int_{R_e}^{\hat{R}} q(R)N(R)dR \right) \quad (S18)$$

$q(R)$

$$= \frac{\pi R^2 \left( \Delta T - \frac{2T_{sat}\sigma}{Rh_{fg}\rho_w} \right)}{\frac{1}{2h_{int}(1 - \cos \theta)} + \frac{R\theta}{4k_w \sin \theta} + \frac{1}{k_{HC} \sin^2 \theta} \left( \frac{k_p \varphi}{\delta_{HC} k_p + h k_{HC}} + \frac{k_w(1 - \varphi)}{\delta_{HC} k_w + h k_{HC}} \right)^{-1}} \quad (S19)$$

where  $q''$  is the steady state dropwise condensation heat transfer rate per unit area of the condensing surface,  $\Delta T$  is the temperature difference between the saturated vapor and sample outer surface ( $\Delta T = (T_{sat}(P) - T_s)$ ),  $R^*$  is the critical radius for heterogeneous nucleation ( $R^* = r_c$ ),<sup>6</sup>  $R_c$  is the droplet coalescence radius,  $q(R)$  is the individual droplet heat transfer (Equation S19),  $n(R)$  is the non-interacting droplet size distribution,<sup>5</sup>  $N(R)$  is the coalescence dominated droplet size distribution,<sup>5, 7</sup>  $R$  is the droplet radius,  $\sigma$  is the condensate surface tension,  $h_{fg}$  is the latent heat of phase change,  $\rho_w$  is the condensate density (liquid water),  $\theta$  is the droplet contact angle,  $h_{int}$  is the interfacial heat transfer coefficient,<sup>8</sup>  $k_w$  is the condensate thermal conductivity,  $k_{HC}$  is the hydrophobic coating thermal conductivity,  $\varphi$  is the structured surface solid fraction (equal to one for the flat surfaces considered here),  $h$  is the structured surface height (equal to zero for flat surfaces), and  $\delta_{HC}$  is the hydrophobic coating thickness ( $\approx 1$  nm).<sup>6</sup> The first integral in Equation S14 represents the heat flux component from droplets smaller than the coalescence

length scale ( $R < R_e$ ), where direct growth by vapor accommodation at the liquid-vapor interface dominates and neighboring droplet coalescence is absent. The second integral represents the component of the heat flux from droplets growing mainly by coalescence with other droplets ( $R > R_e$ ). These two components contribute to the total surface heat transfer per unit area ( $q''$ ). The model results were obtained using experimentally determined droplet departure radii  $\hat{R}$  (see Table S1, above) and contact angles.

Note that the equation above is modified on the lubricant infused surface because lubricant is between the structures on the surface. The appropriate equation for the LIS is:

$$q(R) = \frac{\pi R^2 \left( \Delta T - \frac{2T_{sat}\sigma}{R h_{fg} \rho_w} \right)}{\frac{1}{2h_{int}(1 - \cos \theta)} + \frac{R\theta}{4k_w \sin \theta} + \frac{1}{k_{HC} \sin^2 \theta} \left( \frac{k_P \varphi}{\delta_{HC} k_P + h k_{HC}} + \frac{k_W(1 - \varphi)}{\delta_{HC} k_l + h k_{HC}} \right)^{-1}} \quad (S20)$$

where the  $k_w$  has been changed to  $k_l$  in the right-most section of the denominator. Another important modification to the model for LIS is the alteration of the droplet size distribution for large drops,  $N(R)$ . In previous work on dropwise condensation on flat surfaces, and for the model in the present work used for dropwise condensation on a flat surface, the droplet size distribution has been taken as:

$$N(R) = \frac{1}{3\pi R^2 \hat{R}} \left( \frac{R}{\hat{R}} \right)^{-2/3} \quad (S21)$$

However, recent work by Weisensee et al.<sup>9</sup> has suggested that LIS follow a large droplet size distribution of:

$$N(R) = \frac{1}{3\pi R^3} \quad (\text{S22})$$

based on experimental observation. Therefore,  $N(R)$  presented in Equation S22 above is used when modeling LIS. Finally, the droplet radius at which coalescence-based growth begins to dominate was found to vary between samples. Values of 1  $\mu\text{m}$ , 4  $\mu\text{m}$ , and 8  $\mu\text{m}$  were used for water condensation on the flat hydrophobic surface, water condensation on the LIS, and toluene condensation on the LIS, respectively; all of these values lie in the range of typically observed droplet radii for coalescence dominated growth of 0.5–10  $\mu\text{m}$ <sup>9</sup> and may have implications in the nucleation behaviour of droplets on LIS.

To model filmwise condensation on the smooth Cu tubes, the Nusselt model was used:<sup>4, 8</sup>

$$h_{c,f} = 0.729 \left( \frac{g\rho_w(\rho_w - \rho_v)k_w^3 h'_{fg}}{\mu_w(2r)\Delta T} \right)^{1/4} \quad (\text{S23})$$

$$h'_{fg} = h_{fg} + 0.68c_{p,l}\Delta T \quad (\text{S24})$$

where  $g$  is the gravitational acceleration ( $g = 9.81 \text{ m/s}^2$ ),  $\rho_v$  is the water vapor density,  $\mu_w$  is the condensate dynamic viscosity,  $h'_{fg}$  is the modified latent heat of vaporization accounting for the change in specific heat of the condensate, and  $c_{p,l}$  is the condensate specific heat.<sup>4, 8</sup>

An example of the dropwise and filmwise heat transfer coefficients as a function of condenser subcooling yielded from the above models is plotted in Figure S2 under typical experimental

SI-15

conditions for condensation of water. The dropwise condensation heat transfer coefficient decreases at low subcooling because the interfacial heat transfer coefficient becomes a major resistance to heat transfer.<sup>3b, 10</sup> Meanwhile, the filmwise condensation heat transfer coefficient increases at low subcooling as the film becomes thinner at low heat fluxes<sup>11</sup> (note that, although the heat transfer coefficient is increasing, the heat flux is decreasing). Furthermore, the Nusselt theory used for filmwise condensation does not consider the interfacial heat transfer coefficient, which would decrease the heat transfer coefficient at low subcooling in competition with the increase due to the thinner film. This results in the dropwise and filmwise heat transfer coefficients approaching each other as subcooling decreases.

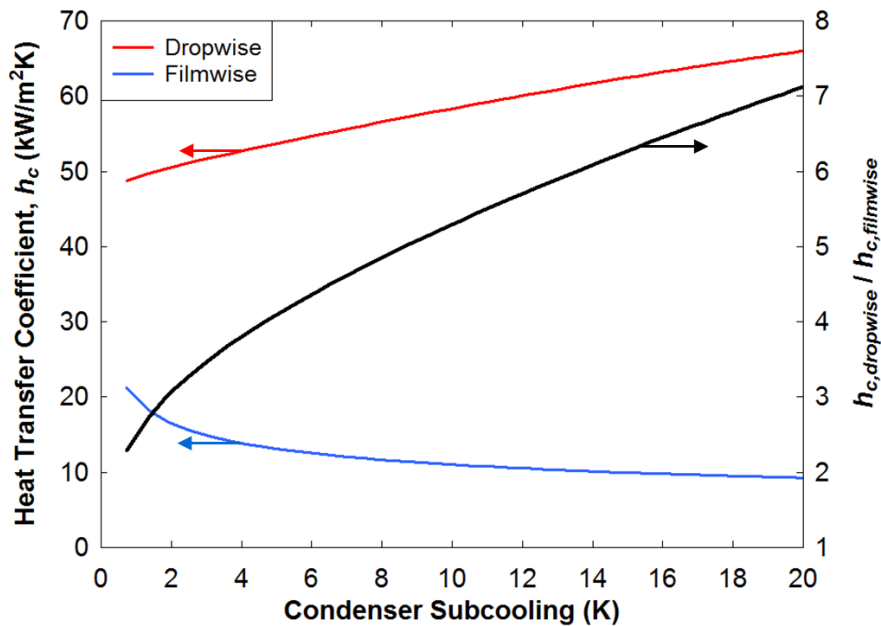


**Figure S2.** Plot of model results for filmwise and dropwise condensation heat transfer coefficient as a function of condenser subcooling, keeping the condenser temperature constant at 15.5 °C ( $P_{sat} = 1780$  Pa) and varying the surrounding saturated water vapor temperature from 16 to 35.5 °C ( $P_{sat} = 1840$  to 5860 Pa). The secondary (right) vertical axis is the ratio of dropwise to filmwise condensation heat transfer coefficients.

In the present study, the condenser subcooling during dropwise condensation of water ranged from  $\approx 1.5$ -6 K. The experimentally determined heat transfer coefficient enhancement of 3-4x for dropwise condensation of water on flat hydrophobic and LIS-coated tubes compared to filmwise condensation is in excellent agreement with the model shown in Figure S2 in the 2-5 K subcooling range where the experimental measurements were taken. Note that, at higher subcooling over  $\approx 10$  K, the typically reported heat transfer coefficient enhancement of up to one order of magnitude<sup>3b</sup> for dropwise compared to filmwise condensation would be realized.

### S7. Lubricant Layer Thickness

The lubricant layer thickness was approximated by dividing the total volume of lubricant added to the surface by the projected surface area of the condenser tube. The total volume of added lubricant was calculated with Equation S25 based on the procedure described in the main text:

$$V_{lub} = n \frac{4}{3} \pi r_{lub}^3 \quad (\text{S25})$$

where  $n$  is the number of droplets of lubricant added to the surface (1 droplet in the present work) and  $r_{lub}$  is the radius of each droplet of lubricant added to the surface (1 mm in the present work). The surface area of the condenser tube is:

$$A_{cond} = 2\pi r_{tube} L_{tube} \quad (\text{S26})$$

where  $r_{tube}$  and  $L_{tube}$  are the radius and the length of the condenser tube, respectively. Then, the thickness of the lubricant layer is:

$$t_{lub} = V_{lub} / A_{cond} \quad (\text{S27})$$

In the present work, this lubricant layer thickness is 1.6  $\mu\text{m}$ , on the same order as the copper oxide nanostructures, which have a characteristic height of 1 to 2  $\mu\text{m}$ .<sup>12</sup> Therefore, the lubricant completely filled the nanostructured surface without significant excess. The thermal resistance

of the lubricant layer was also estimated to determine its effect on the overall heat transfer performance. The thermal resistance is:

$$R_{lub} = t_{lub}/k_{lub} \quad (S28)$$

where  $k_{lub}$  is the thermal conductivity of the lubricant,  $\approx 0.09$  W/m-K for Krytox GPL 101. Therefore, in the present work, the thermal resistance of the lubricant is approximately  $1.8 \times 10^{-5}$  m<sup>2</sup>K/W. Comparing this to the thermal resistances for filmwise condensation of water ( $8.2 \times 10^{-5}$  m<sup>2</sup>K/W) and toluene ( $5.1 \times 10^{-4}$  m<sup>2</sup>K/W), it is clear that, even with the lubricant layer, we can expect a maximum heat transfer enhancement of up to 4.5x for water and 28x for toluene compared to filmwise condensation based on this simplified analysis. In fact, the actual maximum enhancement is greater due to the relatively high thermal conductivity of the copper oxide nanostructures compared to the lubricant, which essentially form a composite material with the lubricant and significantly lower the thermal resistance.

### **S8. Transition to Filmwise Condensation of Toluene**

Although toluene has a finite positive contact angle on the flat hydrophobic condenser, the low value of contact angle and high contact angle hysteresis result in a transition to filmwise condensation even at very low subcooling of less than 1 K, shown in Figure S3 below. This phenomenon has been reported previously, where low-contact-angle fluids typically condense in the filmwise mode.<sup>13</sup>

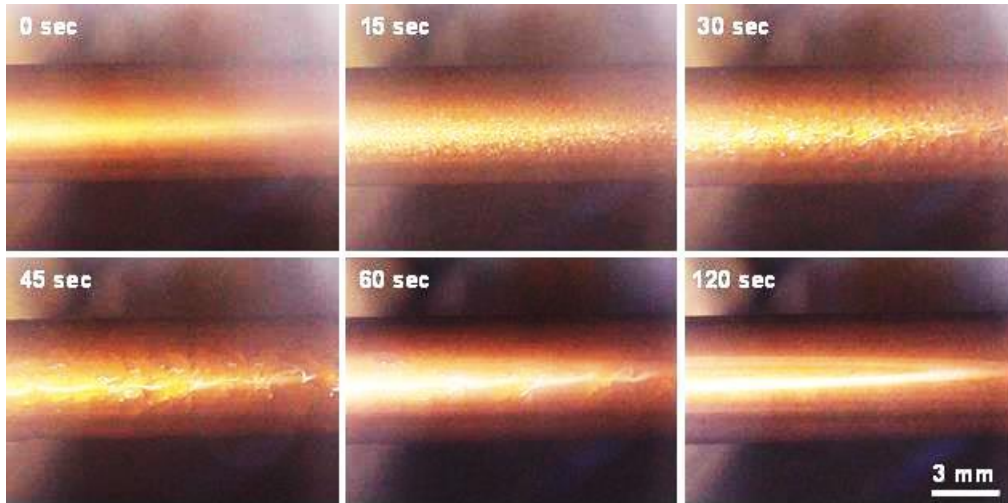


**Figure S3.** *Transition from dropwise to filmwise condensation for toluene condensing on the flat hydrophobic surface. These time-lapse images show that discrete droplets initially form and grow on the surface; however, due to the low contact angle and high contact angle hysteresis, the condensation mode transitions to filmwise even at low ( $<1$  K) subcooling.*

## SUPPLEMENTARY INFORMATION REFERENCES

1. Miljkovic, N.; Enright, R.; Nam, Y.; Lopez, K.; Dou, N.; Sack, J.; Wang, E. N., Jumping-Droplet-Enhanced Condensation on Scalable Superhydrophobic Nanostructured Surfaces. *Nano Lett* **2013**, *13* (1), 179-187.
2. Xiao, R.; Miljkovic, N.; Enright, R.; Wang, E. N., Immersion Condensation on Oil-Infused Heterogeneous Surfaces for Enhanced Heat Transfer. *Sci Rep-Uk* **2013**, *3*, 1988.
3. (a) Ma, X. H.; Zhou, X. D.; Lan, Z.; Li, Y. M.; Zhang, Y., Condensation Heat Transfer Enhancement in the Presence of Non-Condensable Gas Using the Interfacial Effect of Dropwise Condensation. *Int J Heat Mass Tran* **2008**, *51* (7-8), 1728-1737; (b) Rose, J. W., Dropwise condensation theory and experiment: a review. *P I Mech Eng a-J Pow* **2002**, *216* (A2), 115-128.
4. Incropera, F. P., *Introduction to heat transfer*. 5th ed.; Wiley: Hoboken, N.J., 2007; p 901.
5. Miljkovic, N.; Enright, R.; Wang, E. N., Modeling and Optimization of Superhydrophobic Condensation. *Journal of Heat Transfer* **2013**, *135* (11), 111004-111004.
6. Kaschiev, D., *Nucleation: Basic Theory With Applications*. Butterworth Heinemann: Oxford, 2000.
7. Rose, J. W.; Glicksman, L. R., Dropwise condensation - the distribution of drop sizes. *Int J Heat Mass Tran* **1973**, *16*, 411-425.
8. Carey, V. P., *Liquid-vapor phase-change phenomena : an introduction to the thermophysics of vaporization and condensation processes in heat transfer equipment*. 2nd ed.; Taylor and Francis: New York, 2008; p 742.
9. Weisensee, P. B.; Wanga, Y.; Hongliang, Q.; Schultz, D.; King, W. P.; Miljkovic, N., Condensate droplet size distribution on lubricant-infused surfaces. *Int J Heat Mass Tran* **2017**, *109*, 187-199.
10. (a) Wilmshurst, R.; Rose, J. W., Dropwise Condensation—Further Heat Transfer Measurements. In *Fourth International Heat Transfer Conference*, Elsevier: Paris-Versailles, France, 1970; Vol. 6; (b) Enright, R.; Miljkovic, N.; Alvarado, J. L.; Kim, K. J.; Rose, J. W., Dropwise Condensation on Micro- and Nanostructured Surfaces. *Nanoscale and Microscale Thermophysical Engineering* **2014**, *18* (3), 223-250.
11. Nusselt, W., The surface condensation of water vapour. *Z Ver Dtsch Ing* **1916**, *60*, 541-546.
12. (a) Preston, D. J.; Massachusetts Institute of Technology. Department of Mechanical Engineering., *Electrostatic charging of jumping droplets on superhydrophobic nanostructured surfaces : fundamental study and applications*. p 76 pages; (b) Preston, D. J.; Miljkovic, N.; Enright, R.; Wang, E. N., Jumping droplet electrostatic charging and effect on vapor drag. *Journal of Heat Transfer* **2014**, *136* (8), 080909; (c) Bhatia, B.; Preston, D. J.; Bierman, D. M.; Miljkovic, N.; Lenert, A.; Enright, R.; Nam, Y.; Lopez, K.; Dou, N.; Sack, J.; Chan, W. R.; Celanovic, I.; Soljagic, M.; Wang, E. N., Nanoengineered Surfaces for Thermal Energy Conversion. *15th International Conference on Micro and Nanotechnology for Power Generation and Energy Conversion Applications (Powermems 2015)* **2015**, *660*, 012036.
13. Cho, H. J.; Preston, D. J.; Zhu, Y.; Wang, E. N., Nanoengineering materials for liquid–vapour phase-change heat transfer. *Nature Materials Reviews* **2016**, *2*, 16092.